

Bidirectional mixing in an ACE 1 marine boundary layer overlain by a second turbulent layer

Lynn M. Russell,^{1,2} Donald H. Lenschow,² Krista K. Laursen,² Paul B. Krummel,³ Steven T. Siems,⁴ Alan R. Bandy,⁵ Donald C. Thornton,⁵ and Timothy S. Bates⁶

Abstract. In the Lagrangian B flights of the First Aerosol Characterization Experiment (ACE 1), the chemistry and dynamics of the postfrontal air mass were characterized by tracking a constant-level balloon launched into the air mass for three consecutive 8-hour flights of the instrumented National Center for Atmospheric Research C-130 aircraft during a 33-hour period. The boundary layer extended to a height of 400 to 700 m during this period, with its top defined by changes in the amount of turbulent mixing measured rather than by an inversion. Above the planetary boundary layer to a height of 1400 to 1900 m, a second layer was capped with a more pronounced temperature inversion and contained only intermittent turbulence. Since this layer served as a reservoir and mixing zone for boundary layer and free tropospheric air, we have called it a buffer layer to emphasize its differences from previous concepts of a residual or intermediate layer. Estimates of the entrainment rate of dimethyl sulfide (DMS) and aerosol particles between the boundary layer and the buffer layer demonstrated that exchange occurred across the interface between these two layers in both upward and downward directions. In situ measurements of aerosol particles revealed highly concentrated, nucleation-mode aerosol particles between 10 and 30 nm diameter at the beginning of the first Lagrangian B flight in the buffer layer, while few were present in the boundary layer. Observations during the second and third flights indicate that aerosol particles of this size were mixing downward into the boundary layer from the buffer layer while DMS was transported upward. This fortuitous enhancement of aerosol particles in the buffer layer allowed simultaneous use of DMS and aerosol particle budgets to track the bidirectional entrainment rates. These estimates were compared to those from measurements of mean vertical motion and boundary layer growth rate, and from estimates of the fluxes and changes in concentration across the layer interface. In addition, three different techniques were used to estimate DMS emission rates from the ocean surface and showed good agreement: (1) evaluation of the DMS and aerosol mean concentration budgets, (2) seawater DMS concentrations and an air-sea exchange velocity, and (3) the mixed-layer gradient technique.

¹Department of Chemical Engineering, Princeton University, Princeton, New Jersey.

²National Center for Atmospheric Research, Boulder, Colorado.

³Division of Atmospheric Research, Commonwealth Scientific and Industrial Research Organization, Aspendale, Victoria, Australia.

⁴Department of Mathematics, Monash University, Clayton, Victoria, Australia.

⁵Department of Chemistry, Drexel University, Philadelphia, Pennsylvania.

⁶Pacific Marine Environmental Laboratory, National Oceanic and Atmospheric Administration, Seattle, Washington.

Copyright 1998 by the American Geophysical Union.

Paper number 97JD03437.
0148-0227/98/97JD-03437\$09.00

1. Introduction

In the past, studies of convective planetary boundary layer (PBL) structure have been limited mostly to cases where the PBL grows by entraining fluid from an overlying nonturbulent layer into the turbulent PBL by eddies that impinge on the stable interface and incorporate fluid into the PBL. The PBL is perceived as being well-mixed (thus giving rise to the label “mixed layer”) for the region between the surface layer and the capping inversion. This concept has been extended to PBLs with cumulus clouds forming near the top where the latent heat released from condensation allows the newly formed clouds to penetrate the stable interface at the top and transport fluid from the PBL into the overlying layer [Cotton *et al.*, 1995]. By this so-called cloud venting process, a transition layer develops which has prop-

erties intermediate between the PBL and the overlying free troposphere—a lapse rate that is often close to wet adiabatic and profiles of variables that change roughly linearly between PBL values and free-tropospheric values. The daytime PBL over land often seems to follow the scenario of a cumulus cloud transition layer above a well-mixed layer, which late in the day as the convective forcing disappears, forms a “residual layer” which is no longer mixed by cumulus but retains the properties that cumulus mixing has generated during the middle of the day.

Over the ocean, diurnal effects are minimal, and fair-weather cumulus mixing may continue over an extended time with a steady state or slowly varying cloud-mixed transition layer. The upward mixing of water by cumulus convection may be roughly balanced by generally subsiding flow and by mixing of drier air from above through the turbulence generated by the cumulus convection. This type of PBL–cloud layer structure has been documented, for example, by *Albrecht* [1979].

Here we document a marine PBL that has an added level of complexity, which, as far as we know, has not been described previously in the literature. We discuss a case study in which mixing occurs in a layer overlying the classically defined PBL by both clouds and clear-air turbulence. This two-layered structure is characterized by a turbulent lower boundary layer which extends up to 400 to 700 m and is initially clear but later capped with scattered to broken cumulus and stratocumulus clouds; and above this layer a less-well-mixed layer that contains a lower level of intermittent turbulence. This second layer extends up to a capping inversion at about 1400 to 1900 m. Within this layer we see evidence of the reduced mixing in a more laminated vertical structure. Thus this layer does not seem to contain turbulent eddies that extend throughout its depth, as in the PBL, but rather often contains several sublayers with only intermittent coupling by turbulence between them. A layer of clouds often exists at the top of this second layer, and occasional clouds exist as well at other levels within this layer. Initially, the source of turbulence in the lower layer is primarily surface buoyancy flux. Later, as the air passes over cooler water, the buoyancy flux disappears, but the mean horizontal wind increases so that then the primary source of turbulence is shear. The source of turbulence in the second layer is likely a combination of wind shear and, later when clouds formed, penetrating cumulus convection from the PBL.

This two-layered structure is documented using measurements from the National Center for Atmospheric Research (NCAR) C-130 aircraft from the First Aerosol Characterization Experiment (ACE 1) over the ocean south of Australia in November and December 1995. A set of three flights was conducted south and southwest of Tasmania in a quasi-Lagrangian framework using constant level balloons as a tracer of a volume of air within which chemical and physical instruments aboard the airplane measured over a period of 33 hours. Three

unique aspects of the data set that we apply to this study are (1) aerosol backscatter measurements from a lidar system that can be directed either up or down to identify the edges of aerosol layers, (2) measurements of two tracers which can be used to separately measure entrainment from the lower into the upper layer (dimethyl sulfide (DMS)) and from the upper into the lower layer (aerosol spectra), and (3) measurements of the horizontal divergence as a function of height which can be integrated to estimate mean vertical motion at the layer interfaces.

2. Entrainment Relations

The concept of incorporating a layer between the PBL and the free troposphere follows on the work of *Albrecht* [1979], who dealt with the trade wind boundary layer. Here we generalize this approach to the case where a turbulent layer, which may contain turbulence generated by both clear-air (that is, wind shear) and cloud processes, overlies a classical PBL, as illustrated in Figure 1. We refer to this second layer as a buffer layer. In this case, we do not consider the buffer layer to be part of the PBL, as the PBL is characterized by a mixing time of less than an hour [*Stull*, 1988]. The interface between the two layers is assumed to be infinitesimal compared to the depth of the layers, and a similar interface exists at the top of the buffer layer. Since the buffer layer is turbulent, it too can entrain fluid from both the underlying PBL and the overlying free troposphere. This concept of bidirectional entrainment has been studied via laboratory experiments by *Turner* [1968], and more recently both theoretically and experimentally by *Fernando and Hunt* [1997], and *McGrath et al.* [1997].

We can estimate the magnitude of the two entrainment rates by applying the budget equation to either one tracer, if both its internal sources and boundary fluxes are known for both layers, or, as is the case here, two tracers: one for each layer. In addition, the tracers must have a measurable concentration difference between the two layers. We derive these relations using

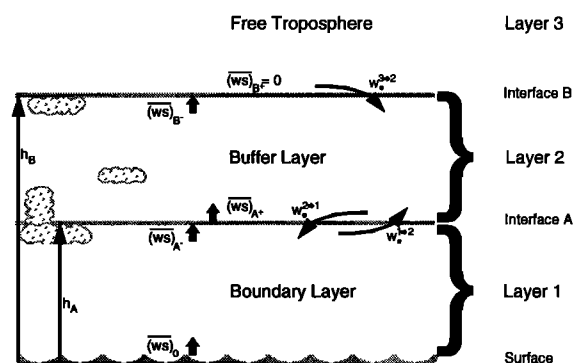


Figure 1. Diagram of the two-layered lower tropospheric structure observed during Lagrangian B.

the budget equation for a scalar $S = S + s$, where S is the mean concentration and s is the fluctuation from the mean:

$$\frac{\partial S}{\partial t} + \frac{\partial \overline{ws}}{\partial z} + W \frac{\partial S}{\partial z} = Q_s \quad (1)$$

where \overline{ws} (the vertical eddy flux of S) is the average of the product ws over a time period long enough to give an accurate statistical average, Q_s is the internal (chemical) source or sink of S , and W is the mean vertical velocity at some level z . In this equation we assume horizontal homogeneity in the turbulence quantities and a Lagrangian framework for the measurements; that is, that the airplane measurements are advected with the mean wind so that there is no mean horizontal advection.

We can integrate this relation between two levels z_1 and z_2 to obtain

$$\left\langle \frac{\partial S}{\partial t} \right\rangle + \frac{(\overline{ws})_{z_2} - (\overline{ws})_{z_1}}{\Delta z} + \langle W \rangle \frac{(S_2 - S_1)}{\Delta z} = \langle Q_s \rangle \quad (2)$$

where $\langle \rangle$ denotes an averaged quantity over the height interval $\Delta z = z_2 - z_1$. In general, a mean fluid motion over the height interval Δz may exist, but normally the mean concentration difference $S_2 - S_1$ is small in regions where mixing occurs so that the mean motion term can be neglected. We define a net entrainment velocity as the net rate at which fluid passes from one layer to another across a jump δS . Thus we allow fluid to pass in both directions between the two layers. We assume that the jump occurs over an infinitesimal layer which we call interface A between the two layers of finite thickness. This velocity is equal to the difference between the time rate of change of the layer interface $\partial h_A / \partial t$ and the mean vertical motion at the height of the interface, W_{h_A} , that is:

$$w_e^A = \frac{\partial h_A}{\partial t} - W_{h_A}. \quad (3)$$

Then, integrating the first term of (1) across this layer and applying Leibnitz's rule gives

$$\int_{z_{A-}}^{z_{A+}} \frac{\partial S}{\partial t} dz = \frac{\partial}{\partial t} \int_{z_{A-}}^{z_{A+}} S dz - \delta S_A \frac{\partial h_A}{\partial t} \quad (4)$$

where z_{A-} and z_{A+} are levels just above and just below the jump and $\delta S_A = S_{A+} - S_{A-}$.

For an infinitesimal thickness of the entrainment zone $z_{A+} - z_{A-}$, the first term on the right side of (4) can be neglected. Then integrating the other terms of (1) across the jump, the source/sink term can also be neglected. Substituting (3) into the result, we have for the integrated budget equation

$$\delta \overline{ws}_A = \left(\frac{\partial h_A}{\partial t} - W_{h_A} \right) \delta S_A = w_e^A \delta S_A, \quad (5)$$

where

$$\delta \overline{ws}_A = (\overline{ws})_{z_{A+}} - (\overline{ws})_{z_{A-}}. \quad (6)$$

Each of the fluxes on the right side of equation (6) can be expressed as a characteristic velocity $\times \delta S_A$. This velocity is a measure of the rate at which fluid is entrained from one side of the jump to the other. Therefore we define two entrainment velocities across interface A, both defined to be positive for a case with mixing in both upward and downward directions, where

$$w_e^{1 \rightarrow 2} = - \frac{(\overline{ws})_{z_{A+}}}{\delta S_A} \quad (7)$$

is in the upward direction and

$$w_e^{2 \rightarrow 1} = - \frac{(\overline{ws})_{z_{A-}}}{\delta S_A} \quad (8)$$

is in the downward direction, as illustrated in Figure 1. Inserting these relations into equation (5),

$$w_e^{2 \rightarrow 1} \delta S_A - w_e^{1 \rightarrow 2} \delta S_A = w_e^A \delta S_A \quad (9)$$

or

$$w_e^{2 \rightarrow 1} - w_e^{1 \rightarrow 2} = w_e^A. \quad (10)$$

We will use the situation illustrated schematically in Figure 1 to analyze the data collected during the ACE 1 Lagrangian B flights. The entrainment across the top of the buffer layer (interface B) is given by

$$w_e^{3 \rightarrow 2} = - \frac{(\overline{ws})_{z_{B-}}}{\delta S_B}. \quad (11)$$

Since $w_e^{2 \rightarrow 3} = 0$, we obtain

$$w_e^{3 \rightarrow 2} = w_e^B. \quad (12)$$

Substituting (8) into (2), and setting $z_1 = 0$ and $z_2 = h_{A-}$, where h_A is the depth of the lower layer, gives

$$\left\langle \frac{\partial S}{\partial t} \right\rangle_1 - \frac{w_e^{2 \rightarrow 1} \delta S_A + (\overline{ws})_0}{h_A} = \langle Q_s \rangle_1. \quad (13)$$

Likewise, substituting (7) into (2), setting $z_1 = h_{A+}$ and $z_2 = h_{B-}$, and applying the same procedure as in (13) to the interface capping layer 2 gives

$$\left\langle \frac{\partial S}{\partial t} \right\rangle_2 - \frac{w_e^{3 \rightarrow 2} \delta S_B - w_e^{1 \rightarrow 2} \delta S_A}{h_B - h_A} = \langle Q_s \rangle_2. \quad (14)$$

These relations can then be solved for the respective entrainment velocities:

$$w_e^{2 \rightarrow 1} = \frac{h_A (\langle \frac{\partial S}{\partial t} \rangle_1 - \langle Q_s \rangle_1) - (\overline{ws})_0}{\delta S_A} \quad (15)$$

$$w_e^{1 \rightarrow 2} = \frac{(h_B - h_A) (\langle Q_s \rangle_2 - \langle \frac{\partial S}{\partial t} \rangle_2) + w_e^{3 \rightarrow 2} \delta S_B}{\delta S_A}. \quad (16)$$

In the case of a classical one-layer convective PBL, the entrainment is assumed to be only from the free troposphere into the PBL. That is, $w_e^{1 \rightarrow 2} = 0$, and $w_e^A = w_e^{2 \rightarrow 1}$. We note that this approach (which we call the budget method) can be generalized to more than two

layers, with similar equations written for the entrainment velocities in both directions between each layer. Thus, if we know the layer thickness, the time rates of change in concentration, the internal source/sink terms and the boundary fluxes for a scalar species, we can estimate the two entrainment rates. Alternatively, if not all of those terms are known for one species in both layers, we may be able to use a separate tracer for each velocity.

In addition to estimating the two separate entrainment rates (by equations (15) and (16)), as well as the net entrainment rate by (5), another approach to measuring the net entrainment rate (which we call the divergence method), for example at h_A , is by measuring the mean vertical motion at the height of the interface, W_{h_A} , as well as the time rate of change of the layer interface, $\partial h_A / \partial t$. The net entrainment w_e^A is given by equation (3). As discussed by Lenschow [1996], W_{h_A} can be obtained by measuring the mean horizontal divergence at several levels below the interface at h_A . The divergence can be obtained from the continuity equation for an incompressible fluid,

$$\frac{\partial \tilde{w}}{\partial z} = -\frac{1}{\mathcal{A}} \oint v_n dl, \quad (17)$$

where \mathcal{A} is the area enclosed by the closed integration path, \tilde{w} is the area-averaged vertical velocity within the integration path, v_n is the horizontal velocity component normal to the path of integration, and dl is the differential path segment. Assuming zero mean vertical velocity at the surface, the mean vertical velocity at h_A can then be estimated by integrating equation (17) from the surface to h_A :

$$W_{h_A} = \int_0^{h_A} \frac{\partial \tilde{w}}{\partial z} dz = - \int_0^{h_A} \left(\frac{1}{\mathcal{A}} \oint v_n dl \right) dz. \quad (18)$$

3. Measurements

We apply the results of the previous section to the measurements obtained from the C-130 aircraft for the second Lagrangian period (flights 24–26 on December 7–9, 1995) of ACE 1. The second Lagrangian experiment was initiated after a precursor survey flight (flight 23) of a frontal passage due west of the northwestern tip of Tasmania. An analysis of the expected trajectory of the postfrontal air revealed that the PBL air would not pass over land and that it would stay within a reasonable range of the ACE 1 base at Hobart airport (Hainsworth *et al.*, this issue). The flight plan employed a series of 60-km diameter stacked circles which were advected with the local wind and reoriented at the top of each stack to the trajectory of a constant level tetron launched from the R/V *Discoverer* [Lenschow, 1996; Huebert *et al.*, 1996; Bates *et al.*, this issue (a)]. The resulting series of measurements seem to have tracked the air mass effectively for the three consecutive research

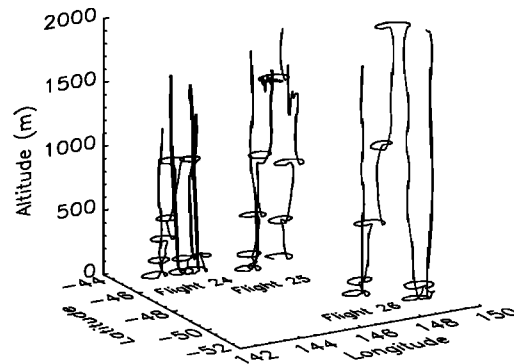


Figure 2. Track plot of NCAR C130 flight path during Lagrangian B, that is, ACE 1 flights 24–26 from 2000 December 7 to 0200 December 9, 1995 (UT). The altitude is measured by a pressure altimeter and contains some noise fluctuations.

flights plotted in Figure 2. The measurements from the aircraft soundings and sequential circles have been used to follow the temporal evolution of the observed boundary layer structure.

The observations carried out during this experiment provide a data set that is complete enough that we can estimate the two separate entrainment velocities by the budget method using equations (15) and (16) with two separate tracers. In addition, we can estimate the net entrainment rates w_e^A and w_e^B with two other independent techniques by (1) using equation (5), with tracers for which we have direct flux measurements (water mixing ratio, virtual potential temperature, and ozone) and (2) estimating the two terms on the right side of equation (3) (the divergence method). The vertically pointed lidar measurements from transects and circles above or below the layers can be used to measure the height of layer boundaries from the local maximum in the backscatter reflectivity gradient. In addition, direct measurement of scalars during vertical airplane soundings can also be used to identify layers. Conducting these measurements over an extended period of almost two days in a Lagrangian framework allows us to evaluate the time rates of change of the layer interfaces. The circular flight patterns flown at several levels within the PBL can be used to measure W_{h_A} and W_{h_B} from equation (18). From these measurements we can estimate the net entrainment rate at interface A, w_e^A , and, assuming unidirectional entrainment, the downward entrainment rate at interface B, $w_e^{3 \rightarrow 2}$, which is used in equation (16).

We use two tracers for estimating entrainment by equations (15) and (16): the spectrum of submicron aerosol particles and DMS concentration. The former is useful for estimating $w_e^{2 \rightarrow 1}$ via equation (15) since the aerosol sources and sinks (for example, surface deposition) in layer 1 are small and easily calculated. It is not useful for layer 2 since aerosols are produced there at a rate that we cannot evaluate. The large magnitude of this entrainment rate compared to estimates of the net

entrainment rate w_e^A by the flux technique provided us with the first evidence that the entrainment process in this case was bidirectional.

On the other hand, the DMS concentration, whose sole source is emission from the ocean and whose atmospheric sink is reaction with OH (which was measured simultaneously on the C-130), can be used to estimate $w_e^{1\rightarrow2}$ via equation (16). In this equation, $w_e^{3\rightarrow2}$ is assumed to be the net entrainment velocity; that is, that $w_e^{2\rightarrow3} = 0$, as is assumed at the top of conventional convective PBLs.

These estimates of $w_e^{2\rightarrow1}$ and $w_e^{1\rightarrow2}$ can be substituted in equation (10) to obtain a second estimate of w_e^A which can be compared with that obtained from the direct flux measurements of water vapor and ozone and from the integrated divergence approach. We can also estimate w_e^A from DMS flux obtained from mean concentration measurements via the mixed-layer gradient method.

Further support for the bidirectional entrainment is given by the observations of significant vertical velocity variance in layer 2 even in the clear-air segments of the flight path. To elucidate the causes of the turbulence in this buffer layer, we calculated a bulk Richardson number from the relation

$$Ri_B = \frac{g}{T} \frac{\Delta\theta_v \Delta z}{(\Delta U)^2 + (\Delta V)^2}, \quad (19)$$

where Δ denotes the difference in mean quantities over flight levels at 500 m in layer 1 and 900 to 1200 m in layer 2. We see in Figure 8 that Ri_B decreases with time, which is consistent with the buffer layer becoming less stably stratified and with the observed increase in $w_e^{1\rightarrow2}$ with time.

3.1. Boundary Layer Height Structure

Two independent measurement techniques provided a uniquely detailed picture of the boundary layer structure and its horizontal inhomogeneities. The first was the measurement of aerosol backscatter as a function of distance from the aircraft via lidar which could be operated in both upward and downward looking modes to provide observations of the lower and upper boundaries of both clouds and aerosol layers in the manner described by Schwesow *et al.* [1990]. The second technique was measurement of vertical profiles via aircraft soundings which provided in situ mean and turbulence measurements of, for instance, temperature, humidity, and vertical velocity to support the layered structure indicated by the lidar. In addition, the appearance of cloud features is studied through measurements of backscatter, precipitation, and cloud droplet concentrations. Details of these techniques are discussed in the following sections.

3.1.1. Lidar data. The Scanning Aerosol Backscatter Lidar (SABL) flown in ACE 1 was designed by Morley *et al.* [1996] and built by Lentec Corporation (Albuquerque, New Mexico). SABL features vibration-

reduced mounting, temperature-controlled avalanche photodiodes and photomultiplier tubes, and narrow band interference filters for reduced noise. The data used here are highly resolved backscatter profile measurements at a sample rate of 1 s^{-1} . The minimum range is 300 m, and the maximum is 10 km.

SABL observations illustrate a complex structure in the lower 2 km of the atmosphere during Lagrangian B. The PBL top, as evidenced by the large decrease in aerosol backscatter over an interval of a few tens of meters or less between about 400 and 700 m, shows considerable variation in height. This variability occurs both on scales of a few kilometers or less, which is indicative of thermals driven by surface buoyancy flux, as well as on tens of kilometers, which is due to mesoscale processes such as sea surface temperature variations (Q. Wang *et al.*, manuscript in preparation, 1998). Below this, the backscatter is uniform, indicating that both aerosol particles and humidity are well-mixed through the PBL (Plate 1a-1c). Variations in the lidar backscatter above the PBL reveal layers of humidity or particle concentrations. These layers appear and persist at levels between 600 and 1400 m. The layered structure suggests that this region is not as well mixed as the PBL, indicating that the turbulence here is not as strong and may be intermittent.

3.1.2. Aircraft soundings. Aircraft soundings through the buffer layer indicate that its chemical composition, water content, and virtual potential temperature are similar to the boundary layer. Figures 3, 4, and 5 illustrate these features during the first flight of Lagrangian B. The similarities in humidity and ozone suggest that the layer had recently been part of the PBL or is being infused with air from the PBL. This layer is similar to a residual boundary layer that forms nocturnally over land when the turbulence can no longer mix up to the height of the temperature inversion capping the daytime PBL in that it has retained the composition although not the same level of turbulent mixing characteristic of a well-mixed PBL. An important difference in this case is that some turbulence persists in this layer at a level sufficient to cause entrainment from both the PBL and the overlying free troposphere, so that it represents a reservoir and mixing zone of both PBL and free-tropospheric air.

The soundings (Figures 3, 4, and 5) indicate three distinct features of the buffer layer: (1) the layer is not well-mixed, (2) the layer is below a strong temperature inversion, and (3) there is intermittent turbulence in the layer. Ozone, humidity, and virtual potential temperature profiles all show indications of layered structures in the buffer layer although a fraction of the layer shows evidence of mixing.

The temperature inversion capping the buffer layer is evident in all soundings across interface B in the virtual potential temperature measurements. Evidence for turbulence appears infrequently in the soundings of vertical velocity, as the most intense high-rate vertical velocity

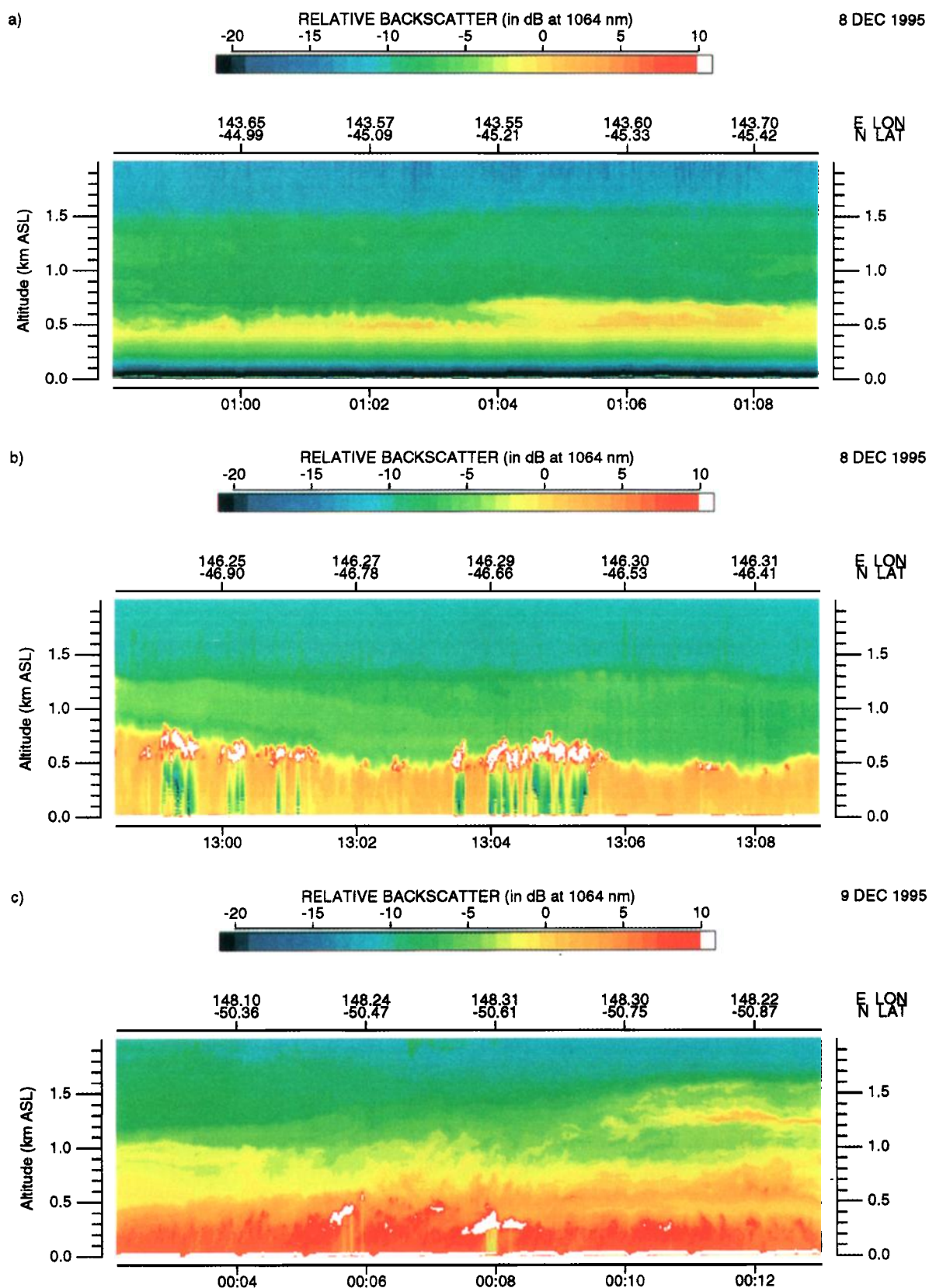


Plate 1. Three lidar images of aerosol backscatter observed during the three flights of Lagrangian B. Each image represents an approximately 11-minute segment of data recorded every other second from the following time segments (in GMT): (a) flight 24, 0058-0110 December 8, 1995; (b) flight 25, 1236-1247 December 8, 1995; (c) flight 26, 0002-0013 December 9, 1995.

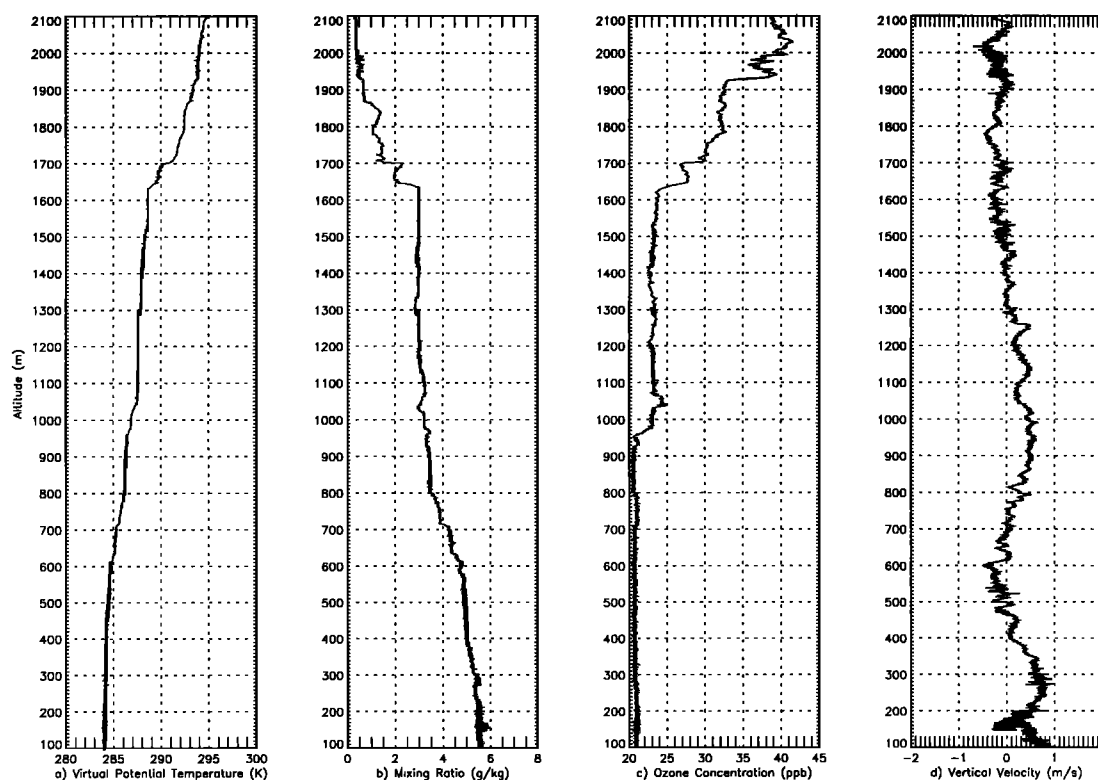


Figure 3. Aircraft sounding during flight 24 at 2128 December 7, 1995, illustrating the vertical distribution of (a) virtual potential temperature, (b) humidity mixing ratio, (c) ozone concentration, and (d) vertical gust velocity.

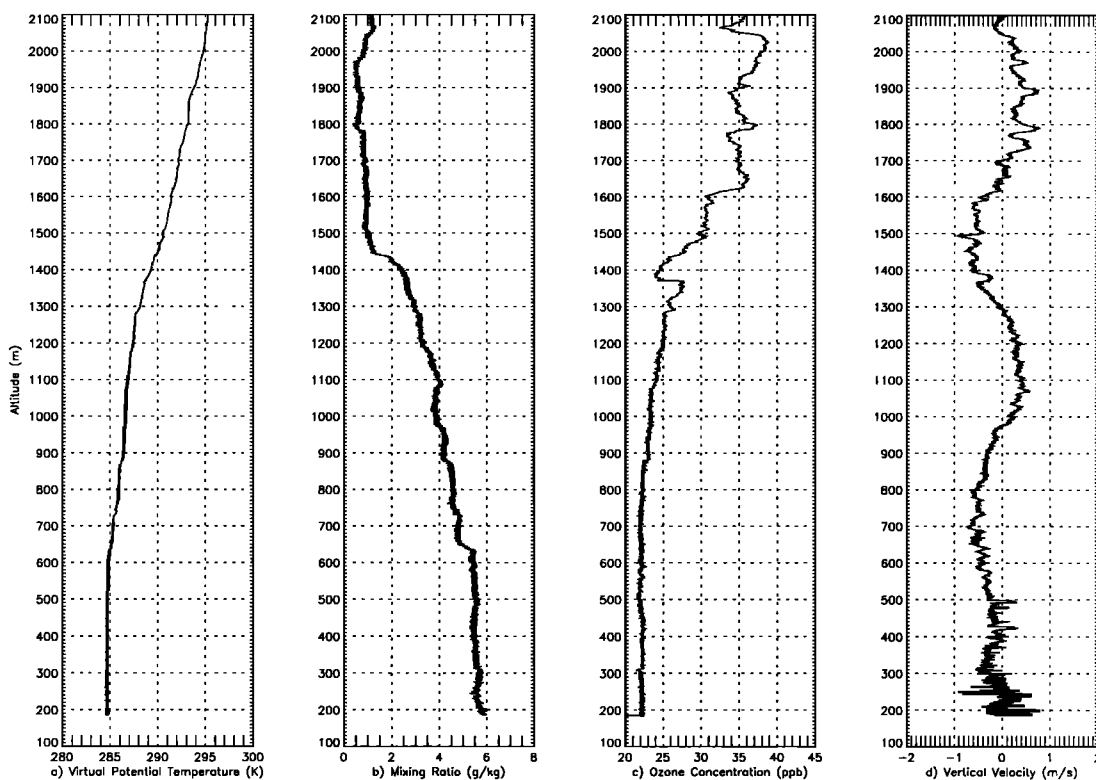


Figure 4. Same as for Figure 3 during flight 25 at 0858 December 8, 1995.

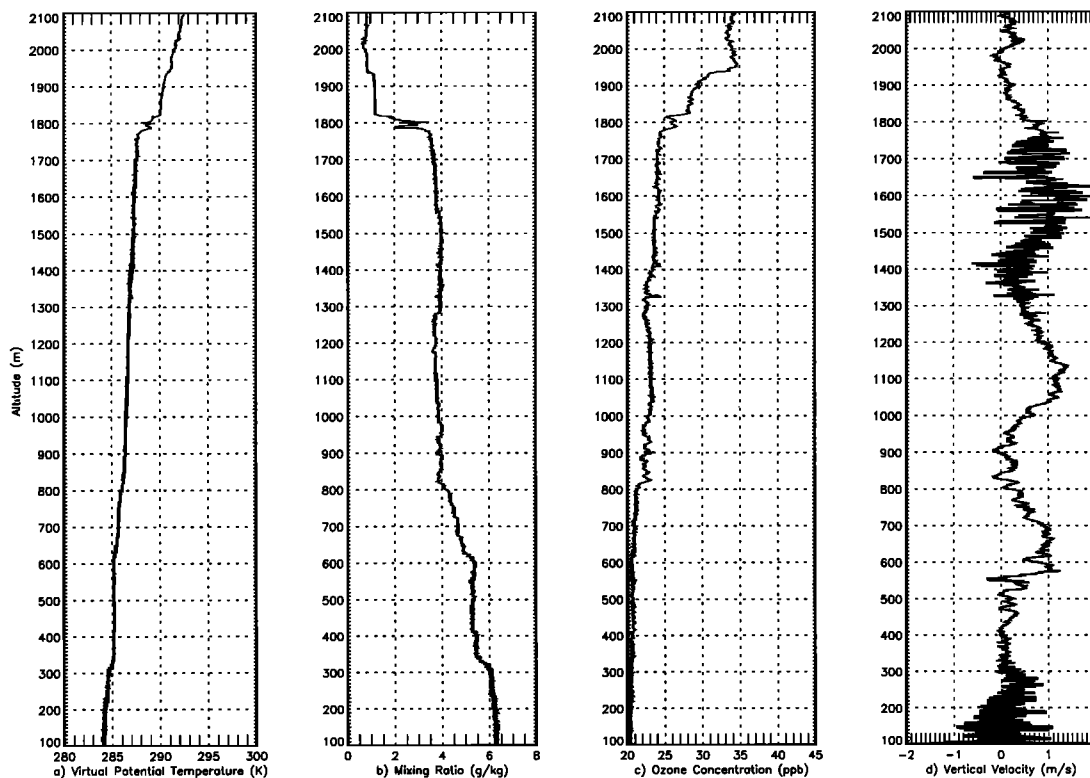


Figure 5. Same as for Figure 3 during flight 26 at 2113 December 8, 1995.

fluctuations end at the top of the boundary layer. However, as discussed in the section on turbulence, several horizontal legs show turbulent fluctuations indicating mixing. The presence of turbulence distinguishes this layer from a continental residual layer in which turbulence is largely absent.

Another distinctive feature of this buffer layer is illustrated by the virtual potential temperature soundings. For example, in Figure 5 (flight 26, December 8, 2204) the virtual potential temperature follows a wet adiabat from 500 to 1000 m. However, from 1000 to 1800 m the air follows a dry adiabat. This characteristic distinguishes the buffer layer structure from the “cloud layer” observed in trade wind regimes [LeMone, 1980], in which a wet adiabat extends through the entire layer to the temperature inversion, indicating that the mixing process in that type of intermediate layer is cloud-driven convection.

3.1.3. Cloud structure. Flight 24 begins the Lagrangian experiment in the early morning in a clear air mass immediately following the passage of a weak cold front. Boundary layer winds are a relatively weak 4 m s^{-1} . Flight 25 is primarily a nighttime flight, so visual confirmation of a clear atmosphere was difficult, but neither cloud droplets nor precipitation were recorded. Lidar images suggest the formation of a very humid layer below interface A that was characterized by backscatter typical of haze-sized droplets but not saturated as is expected for cloud structures. During the following day’s flight 26, clouds appear both below interface A,

at interface B, and in the middle of layer 2. The lowest cloud layer below interface A contains wispy stratus with some linear horizontal orientation and tilt consistent with strong shear. The PBL wind speed increased overnight to over 11 m s^{-1} . Higher cloud layers are variable and intermittent with depths of 50 to 300 m. We note that the lidar images also show increasing aerosol backscatter in the buffer layer through the flights, which strongly suggests that PBL air is being entrained into the buffer layer during this period.

3.2. PBL Height Evolution

The salient features of the PBL and buffer layer persist throughout the Lagrangian experiment, as is illustrated both in the lidar images in Plate 1 and the soundings shown in Figures 3, 4, and 5. The PBL, initially 600 m deep, sinks to 450 m at the end of the study period. In contrast, the height of the buffer layer increases from 1400 to 1900 m.

To obtain an expression for the change in the height of each of these interfaces with time, we have fitted second-order curves to the heights obtained from each of the 14 soundings through the lower interface (interface A) and the 11 soundings through the upper interface (interface B). These data are plotted in Figure 6.

In addition, we have used the lidar imagery to obtain spatially-averaged estimates of h_A . The lidar heights were obtained using a wavelet routine to search for the steepest gradients in the aerosol backscatter for every second pulse for 21 flight segments during flights 24

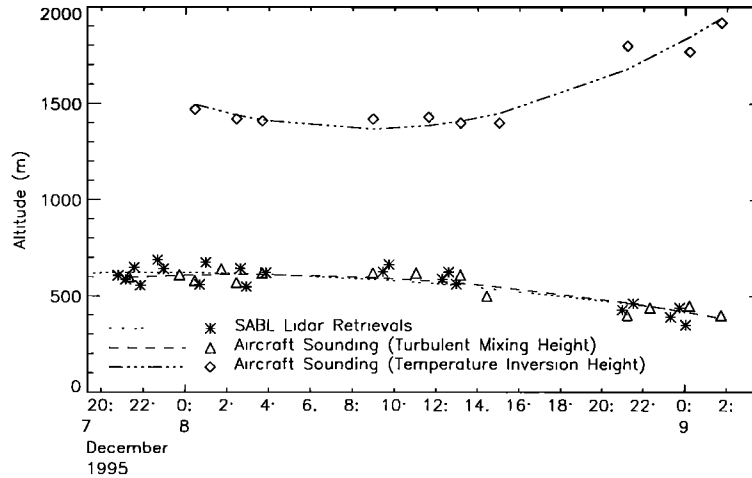


Figure 6. ACE 1 Lagrangian B boundary layer height measurements from SABL lidar data and from aircraft soundings. Asterisks represent SABL lidar data retrievals of the height of the steepest gradient in aerosol backscatter (interface A) using a wavelet algorithm; triangles represent the height of turbulent mixing (interface A) from aircraft sounding data; diamonds show the height of the primary temperature inversion (interface B) measured in aircraft soundings.

through 26. Since the height of the PBL typically varied between 30 and 80 m from the mean through a 30-min circle, as Plate 1 illustrates, a time series of PBL height was very useful for following the trend in the height of interface A. This technique was not successful in estimating the altitude of interface B because of its much weaker backscatter gradient.

Although at several specific times the altitude retrieved from a single sounding was as much as 50 m different from the lidar-retrieved spatial average, the trends in both data sets were nearly identical, as is illustrated by the similarities in the second-order curve fits obtained for both the lidar-wavelet retrievals and the sounding heights (shown in Figure 6). The expressions obtained from these curve fits for the heights of interfaces A from lidar data and B from sounding data, equations (20) and (21), respectively, are

$$h_A(t) = - 2.0007320 \times 10^7 + 1.1703398 \times 10^5 t - 1.7114394 \times 10^2 t^2 \quad (20)$$

$$h_B(t) = + 1.3165369 \times 10^8 - 7.6909641 \times 10^5 t + 1.1232413 \times 10^3 t^2, \quad (21)$$

where t is in Julian Decimal Time (JDT) (2000 December 7 is equivalent to 341.833), h is in meters, and the relationships are defined for $341.8 \leq t \leq 343.1$ days. Differentiating equations (20) and (21) yields the following expressions for the rate of change of the interface height with time:

$$\frac{dh_A(t)}{dt} = \frac{1.1703398 \times 10^5 - 3.4228788 \times 10^2 t}{86400} \quad (22)$$

$$\frac{dh_B(t)}{dt} = \frac{-7.6909641 \times 10^5 + 2.2464826 \times 10^3 t}{86400}, \quad (23)$$

where $dh(t)/dt$ has been converted to m s^{-1} by dividing by 86400 s d^{-1} .

Entrainment in both directions across interface A, namely both of air from layer 2 into layer 1 and from layer 1 into layer 2, requires turbulence in both layers. The turbulence in layer 1 is clearly illustrated by high-frequency fluctuations in the vertical velocity during aircraft soundings below 600 m. We calculate the Obukhov length L to characterize the PBL stability in order to describe the character of the turbulence in this layer. In layer 2, the turbulence is more intermittent, so we discuss both the potential for shear-driven turbulence using a bulk Richardson number Ri_B and specific examples of turbulence measurements.

3.2.1. Obukhov length. Figure 7 illustrates the Obukhov length (L) calculated for the PBL (layer 1), and the ratio h_A/L to provide a measure of the hydrodynamic stability of the PBL. The magnitude of the Obukhov length is proportional to the height at which the rates of shear and buoyancy generation of turbulence are of comparable magnitude. During flight 24 (stacks 1 through 3, from JDT 341.92 to 342.42) this value is negative and decreasing in magnitude, indicating a convective boundary layer in which the relative contribution of buoyancy is increasing. During stacks 4 and 5, $-L$ increases, which indicates a decreasing contribution from buoyancy. During stacks 6 and 7, the buoyancy flux is small and negative, and the friction velocity u_* is doubled, so that L is positive and increasing. (The Obukhov length for stack 5 (at JDT 342.56) was estimated from the 150 m flight level, since no 30 m flight level was available for this stack.) The result is that h_A/L increases from stack 3 through 6 (from JDT

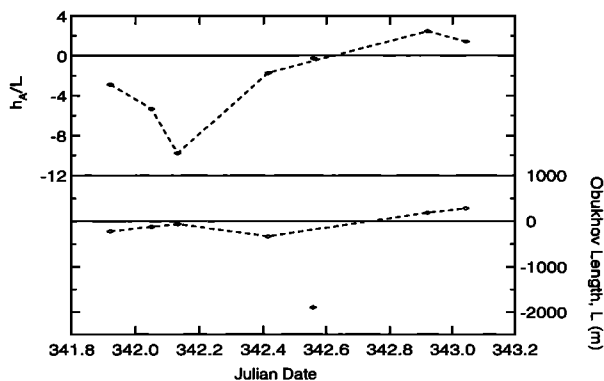


Figure 7. (bottom) The Obukhov lengths L for layer 1 using flux measurements at 30 m are shown by an open diamond for each of stacks 1, 2, 3, 4, 6, and 7 during Lagrangian B; L for stack 5 based on measurements at 150 m is shown with a solid diamond. (top) The ratio of the PBL height to the Obukhov length h_A/L .

342.13 to 342.92) from -9.0 to 0.5, showing a trend from a slightly unstable to a slightly stable PBL.

3.2.2. Richardson numbers. We calculate a bulk Richardson number (equation (19)) plotted in Figure 8 from data in stacks 1 through 7 between the 500 m flight level, to characterize PBL values, and at a level in the buffer layer between 900 and 1200 m to estimate the potential for turbulence generation in the buffer layer. We use the Richardson number as an indication of the likelihood that the observed turbulence is generated by shear rather than by convection. Ri_B is positive and decreasing from 36 to 7 during flight 24 and continues to decrease to less than 1 in flight 26. The continuous wind soundings from all three flights shown in Figure 9 do not vary monotonically between the two flight levels; rather, they show local maxima and minima. Thus the local Richardson number can be considerably less than this integrated value, so it is not surprising that Ri_B never reaches a critical value. Nevertheless, the decreasing Richardson number is consistent with the layer becoming less stable and more likely to have intermittent turbulence.

During flights 24 and 25, no clouds were noted in the buffer layer within the study area, and turbulence was observed intermittently. In flight 26, a few small cumulus clouds were observed, but they covered only a small fraction of the measurement area. Figures 10, 11, and 12 show three examples from flight 26 of high-frequency vertical velocity fluctuations at 30, 1226, and 2133 m. Figure 10 shows turbulence in cloud-free air in the boundary layer. Figure 11 shows that there is turbulence present in cloud-free air in the buffer layer. Figure 12 shows turbulence in cloudy air in the buffer layer.

3.3. Flux Method Calculations

During each circle flown in the boundary layer, humidity, ozone, and virtual potential temperature were

available at a sampling rate of 25 s^{-1} for 30 min covering a distance of approximately 180 km. This measurement rate provides more than enough samples to characterize turbulent transport processes from about 8 m to 10 km in length [Lenschow, 1995]. Cospectra of humidity, ozone, and virtual potential temperature with vertical velocity were calculated and integrated over the wavelength intervals noted. The resulting fluxes $\overline{ws}(z)$ are plotted against altitude for each stack time in Figures 13, 14, and 15.

3.3.1. Temperature flux. The flux of virtual potential temperature, $\overline{w\theta_v}$, shows a decrease with altitude indicative of warming with height in almost all stacks during Lagrangian B in Figure 13. The exception to this trend is stack 5 which shows a small increase in $\overline{w\theta_v}$ with altitude. Stacks 6 and 7 have negative fluxes at the surface, indicating a surface cooler than the air above.

Virtual potential temperature fluxes from the 30-m circles were compared to aerodynamic transfer estimates of the surface virtual potential temperature flux derived from measurements of radiometric surface temperature and estimated surface pressure and saturation as well as the mean wind at 30 m. The values for all three flights agreed within the specified 1 K accuracy of the radiometer measurements. The largest difference occurred on flight 26; to get agreement on that flight required a 1 K shift in the radiometer temperature. The PBL was stably stratified during flight 26, so mixing was less, and consequently the lapse rate is larger.

3.3.2. Humidity flux. The humidity fluxes plotted against altitude in Figure 14 are positive in all cases, consistent with a humidity source at the surface. For flights 24 and 25, the fluxes at 30 m are consistent with

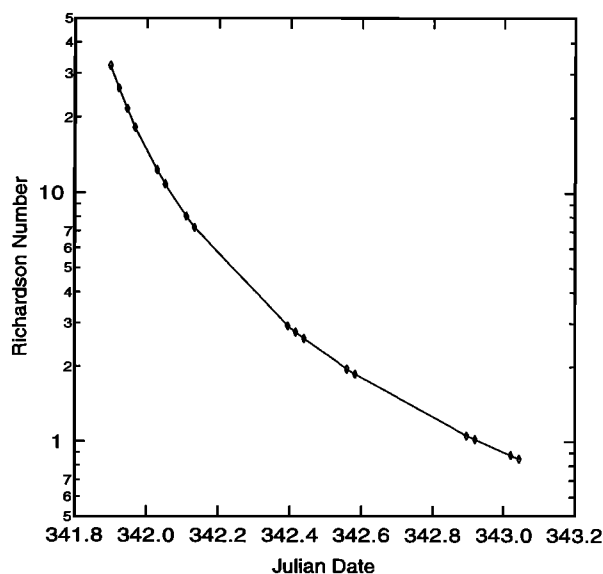


Figure 8. Gradient Richardson number calculated for the buffer layer as a function of time during Lagrangian B.

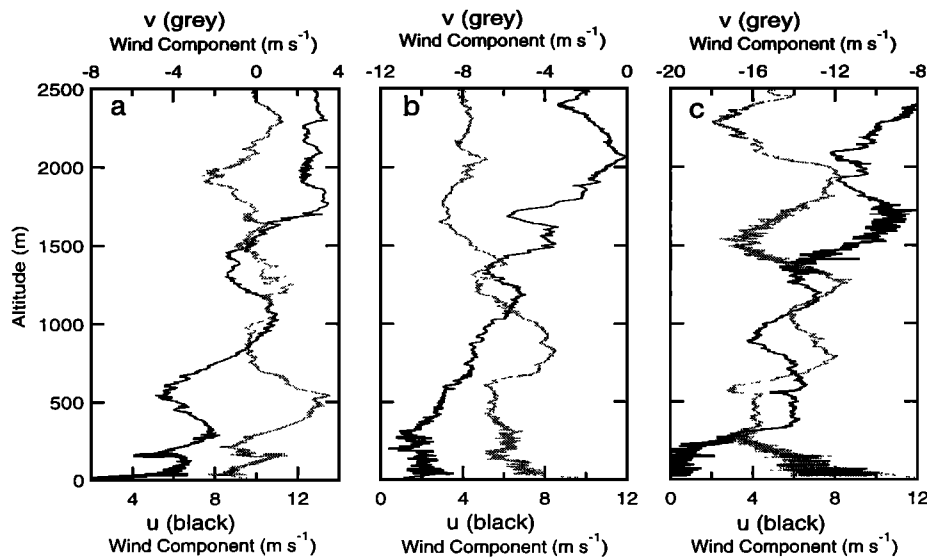


Figure 9. North (grey line) and east (black line) wind components' variation with altitude for soundings in each of the three flights of Lagrangian B, namely (a) flight 24 at 2128 on December 7, 1995, (b) flight 25 at 0858 on December 8, 1995, and (c) flight 26 at 2113 on December 8, 1995.

estimates of the surface flux from the bulk aerodynamic formula, using saturation at the sea surface temperature measured with the surface-temperature radiometer. The comparison for flight 26 indicates lower than expected sea surface temperatures, which are likely to result from an instrument calibration offset discussed above for temperature flux.

3.3.3. Ozone flux. Figure 15 shows negative ozone fluxes throughout the boundary layer, with the first stack indicating values close to zero at interface A. The trend in the magnitude of the entrainment velocity at interface A, shown in Figure 16, follows that predicted from the humidity flux in showing a slow increase from slightly negative (-0.001 m s^{-1}) to a small

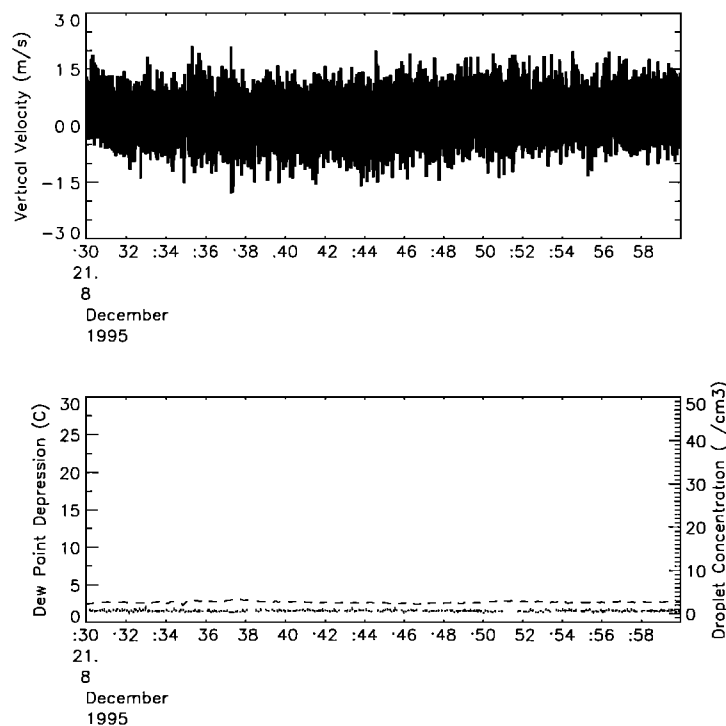


Figure 10. The (top) solid line indicates vertical gust velocity (m s^{-1}), the (bottom) dashed line shows dew point depression (C), and the (bottom) dotted line gives the cloud droplet concentration (Forward Scattering Spectrometer Probe (FSSP), cm^{-3}) at 30 m height during flight 26 at 2130–2200 December 8, 1995.

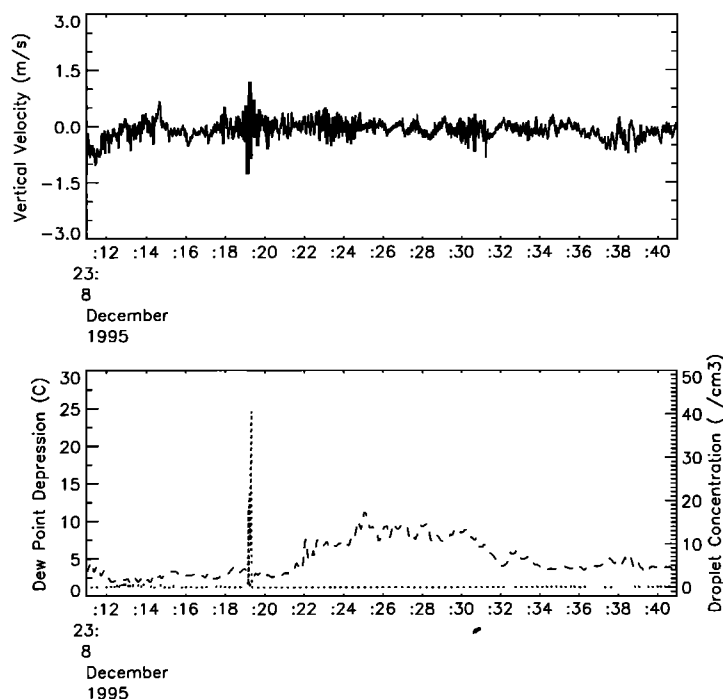


Figure 11. Same as for Figure 10 at 1226 m height during flight 26 at 2311–2341 December 8, 1995.

positive value of 0.003 m s^{-1} for stacks 1, 4, 6, and 7. Stacks 2, 3, and 5 predict entrainment velocities higher than this trend.

3.3.4. Flux-derived entrainment rates. The values in the PBL were extrapolated to h_A using a linear fit to give $\overline{ws}(h_A-)$. Dividing by the jump at the in-

terface, δS_A , provided the values in Figure 16 for $w_e^{2 \rightarrow 1}$. Similarly, Figure 17 shows the analogous calculation for $w_e^{1 \rightarrow 2}$ and Figure 18 shows that for $w_e^{3 \rightarrow 2}$.

For each tracer, the jump at the interface was estimated by two methods. The first provides an upper bound by using

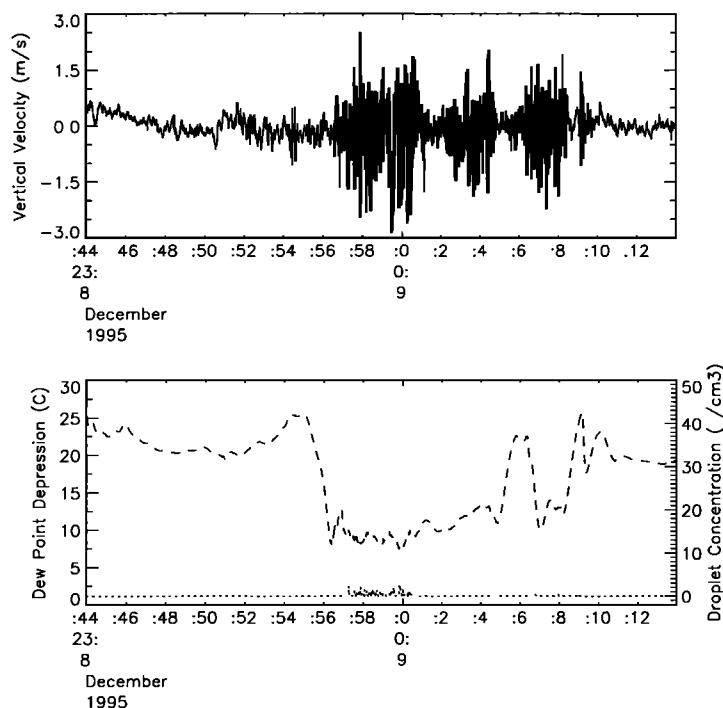


Figure 12. Same as for Figure 10 at 2133 m height during flight 26 at 2344–0014 December 8–9, 1995.

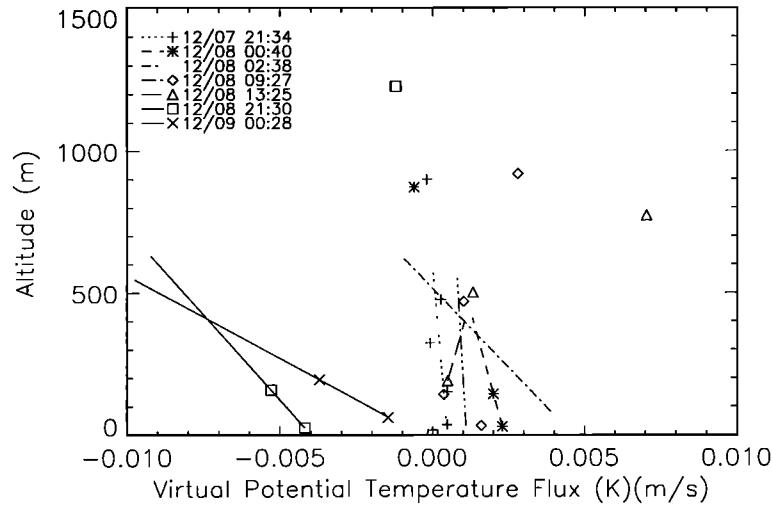


Figure 13. Virtual potential temperature fluxes during Lagrangian B. Each line represents a linear fit to data in the PBL during a single stack of measurements, and each data point represents a flux value calculated from measurements during a 30-min circle.

$$\delta S_A = S_{900 \text{ m circle}} - S_{150 \text{ m circle}}. \quad (24)$$

If S varies monotonically over this range of $\Delta z = 900 - 150$ m, then δS_A is overestimated. An accurate instantaneous but spatially varying measure of the jump in S at interface A was estimated from an aircraft sounding across interface A, such that

$$\delta S_A = \frac{\int_A^{A+\delta z} S dz - \int_{A-\delta z}^A S dz}{\delta z}, \quad (25)$$

where we use $\delta z \approx 50$ m to obtain a sufficient sample for an average value.

We have only one stack during Lagrangian B (12/8 2130) where there are two circles from which we can

extrapolate to $(\overline{ws})_{z_{B-}}$ and $(\overline{ws})_{z_{A+}}$. We will denote these two measurements as $(\overline{ws})_{h_j}$ and $(\overline{ws})_{h_k}$. Therefore we will use the assumption that the gradient of the flux in the buffer layer is constant during Lagrangian B, so that

$$(\overline{ws})_{z_{B-}}(t) \approx m_2(z_{B-} - h_j) + (\overline{ws})_{h_j}(t) \quad (26)$$

$$(\overline{ws})_{z_{A+}}(t) \approx m_2(z_{A+} - h_j) + (\overline{ws})_{h_j}(t) \quad (27)$$

where

$$m_2 \equiv \frac{(\overline{ws})_{h_k} - (\overline{ws})_{h_j}}{h_k - h_j}. \quad (28)$$

For this particular case, we note that the slope m_2 turns out to be small, so we can simplify equations (26) and (27) to

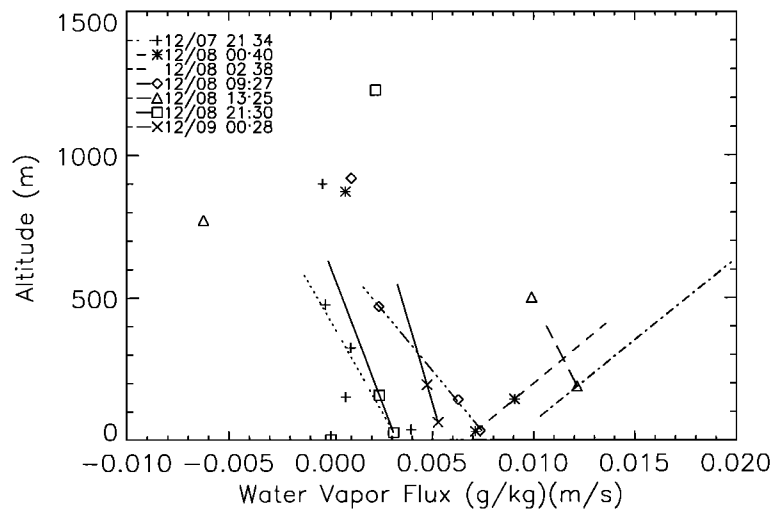


Figure 14. Humidity fluxes during Lagrangian B. Each line represents a linear fit to data in the PBL during a single stack of measurements, and each data point represents a flux value calculated from measurements during a 30-min circle.

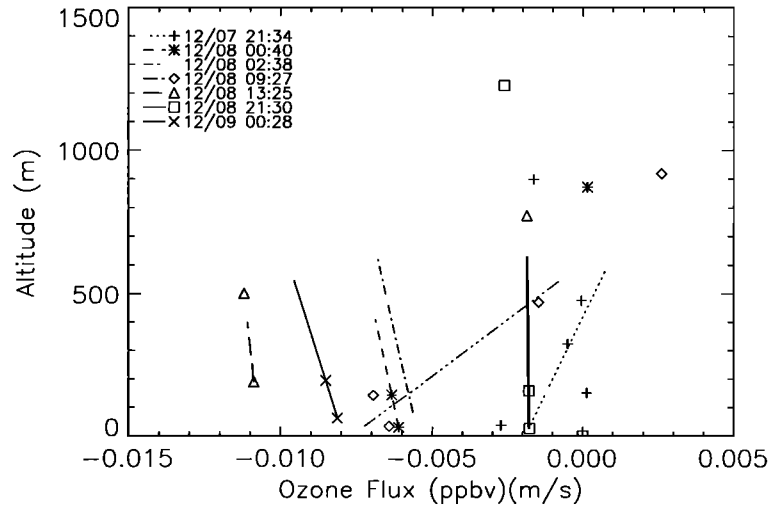


Figure 15. Ozone fluxes during Lagrangian B. Each line represents a linear fit to data in the PBL during a single stack of measurements, and each data point represents a flux value calculated from measurements during a 30-min circle.

$$(\overline{ws})_{z_{B-}} \approx (\overline{ws})_{z_{A+}} \quad (29)$$

In conjunction with equations (7) and (11), Equation (29) leads to

$$w_e^{3 \rightarrow 2} = \frac{\delta S_A}{\delta S_B} w_e^{1 \rightarrow 2} \quad (30)$$

The approximations in equations (26) and (27) are used to provide an estimate of the variation of $w_e^{3 \rightarrow 2}$ with time which can be compared with the estimate based on the relation

$$w_e^B = w_e^{3 \rightarrow 2} = \frac{\partial h_B}{\partial t} - W_{hB} \quad (31)$$

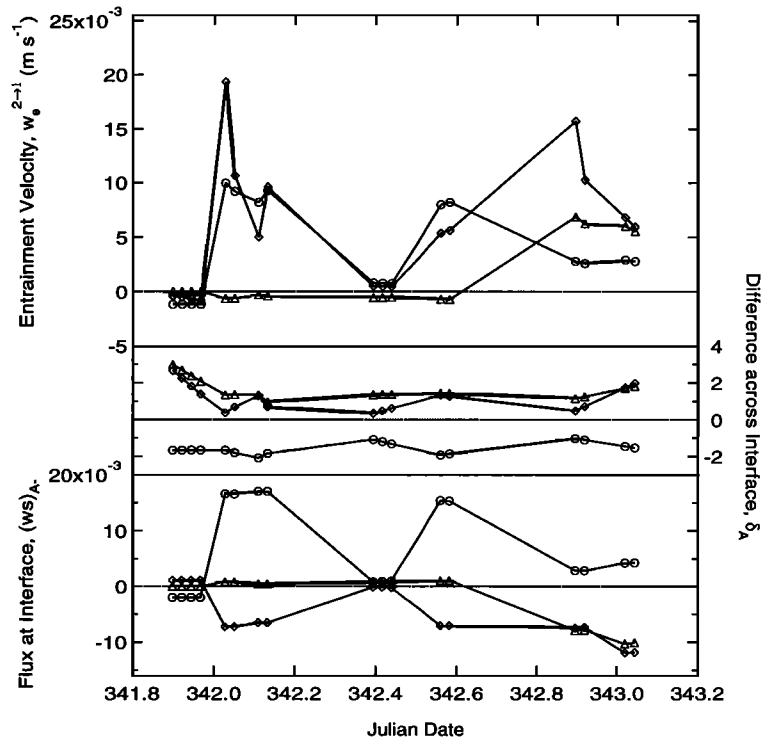


Figure 16. The top panel shows entrainment velocity, $w_e^{2 \rightarrow 1}$, calculated at interface A from estimates of the fluxes of virtual potential temperature, humidity, and ozone. The other two panels show the two quantities from which this velocity is derived, namely the value of the flux at the interface in the bottom panel and the difference in concentration across the interface in the middle panel. Triangles represent virtual potential temperature, circles represent humidity, and diamonds represent ozone measurements.

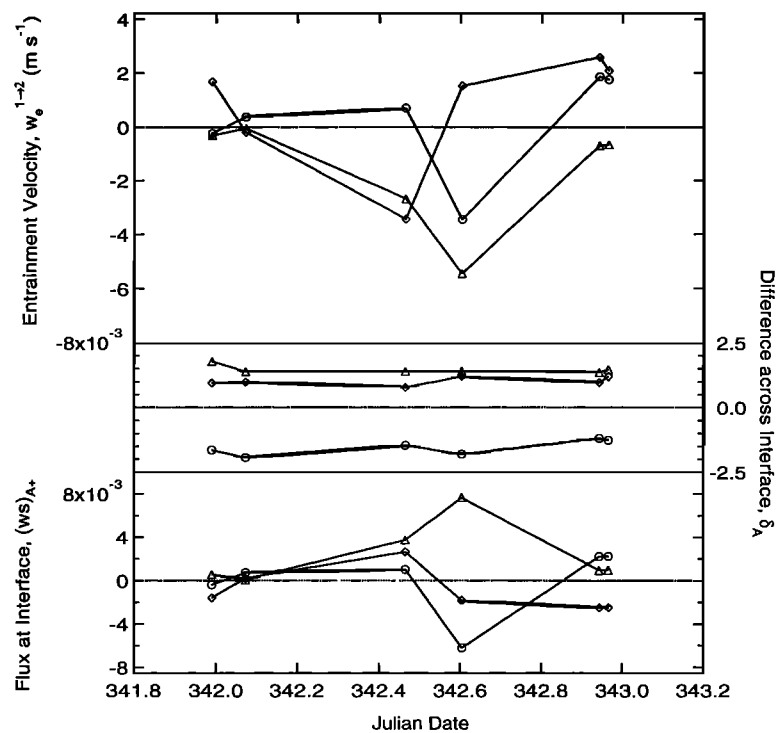


Figure 17. Same as for Figure 16 for the entrainment velocity $w_e^{1 \rightarrow 2}$.

The entrainment velocities calculated from the three flux methods at interface A are shown in Figures 16, 17, and 18. Stacks 1, 4, 6, and 7 indicate \overline{wq} increasing from slightly negative (-0.001 m s^{-1}) to slightly positive

(0.002 m s^{-1}) throughout the duration of Lagrangian B. Stacks 2, 3, and 5 predict larger w_e , between 0.006 and 0.008 m s^{-1} , indicative of the stronger fluxes measured in those stacks.

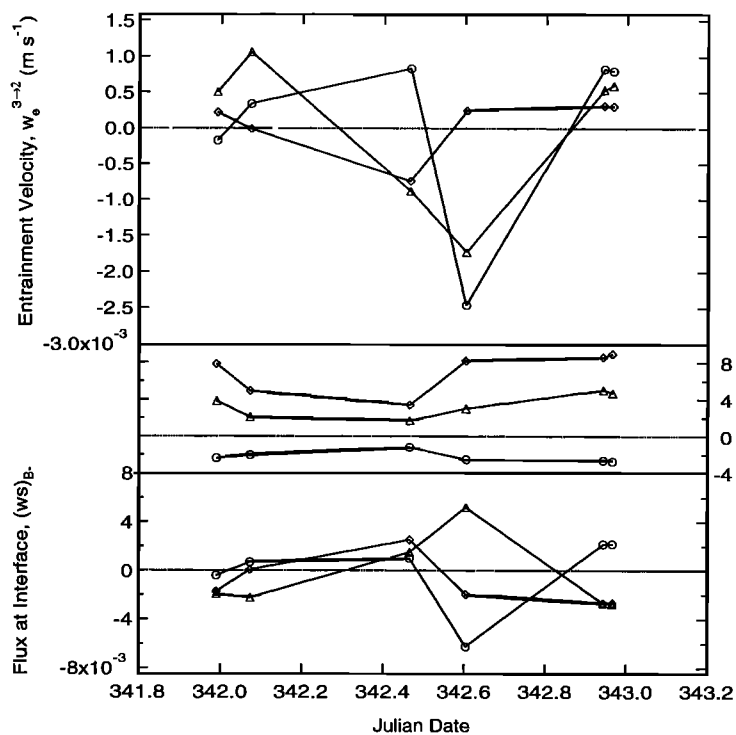


Figure 18. Same as for Figure 16 for the entrainment velocity, $w_e^{3 \rightarrow 2}$.

3.4. Budget Methods

The two budget analyses for interpreting the PBL exchange rates described here were made possible by an extensive and unique complement of submicron aerosol and chemical (DMS and OH) measurements. Results from this method provided the critical evidence for the bidirectional entrainment illustrated in Figure 1. Owing in part to the complex nature of the boundary layer studied in this case, the characterization of turbulent transport without these data would have been incomplete.

3.4.1. Aerosol transport. Measurements of dried submicron aerosol size distributions were collected at 1-min intervals aboard the NCAR C130 using the radially classified aerosol detector (RCAD) system developed by Russell *et al.* [1996]. These measurements were averaged during each circle of Lagrangian B to provide the size distributions in Figure 19. The size distributions above interface B are typical of the free troposphere, containing a single, broad mode at 35–40 nm dry diameter. In the buffer layer, the size distributions all are bimodal, with one peak at 45 nm and the other between 10 and 20 nm dry diameter. In the PBL at both 30 and 150 m, the aerosol size distribution contains a primary mode peak at 45 nm, indicating well-mixed aerosol in the boundary layer and consistent aerosol characteristics throughout the Lagrangian flights.

Both of the sets of circles in the PBL also show the appearance of a second mode peak at 20 nm during the end of flight 25 and its growth throughout flight 26. Since the particles appear in the middle of the Lagrangian at a size range an order of magnitude larger than particles nucleated from gases (typical critical diameters for particles nucleated in the atmosphere are thought to be 1–3 nm diameter), there is little chance that these particles were produced in layer 1 from gaseous precursors. Such production would have been accompanied by observations of growth of the mode from larger numbers of smaller-sized particles during the hours previous to their appearance at 20 nm, since typical observed rates of particle growth by condensation are of the order of several hours for volume doubling, even in more highly concentrated vapor conditions characteristic of polluted air masses. At 20 nm the particles in the new mode are also almost an order of magnitude smaller than the size range expected for sea-salt particle sources (typically observed in significant numbers down to 100 nm).

There are important aerosol dynamic processes that can be particle sinks in this size range, but not sources. Dry deposition will continuously remove particles at a rate proportional to their concentration. However, the loss rate is minimal. For example, 100 nm diameter particles at a concentration of 300 cm^{-3} will lose only $5.2 \times 10^{-7} \text{ cm}^{-3} \text{ s}^{-1}$. For a 500 m boundary layer this gives an e -folding time of almost 20 years. Coagulation cannot result in the creation of new particles in this

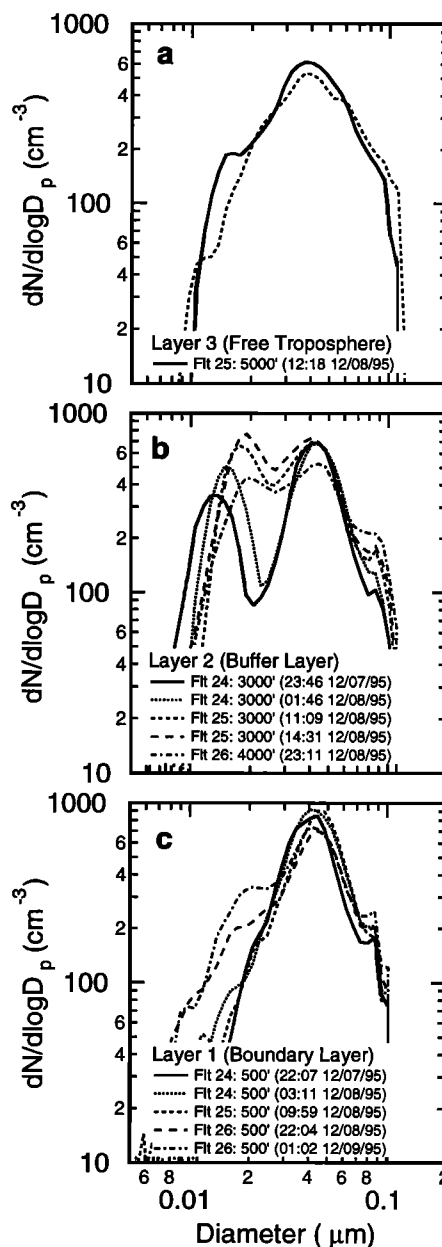


Figure 19. RCAD aerosol size distribution measurements from circles at (a) 1500 m and above, (b) 900 to 1200 m, and (c) 150 m. Each distribution represents the average size distribution of 30 measurements collected at 1-min intervals around a constant-altitude circle.

size range, since there are negligible concentrations of particles of smaller sizes that would result in particles in the 20 nm mode. However, particles in this mode can be lost by coagulation with other particles in this mode as well as with particles in larger modes. The maximum rate of such losses by coagulation for the size distributions considered here under subsaturated conditions is $0.01 \text{ cm}^{-3} \text{ s}^{-1}$, which gives an e -folding time of about 8 hours for a 500 m deep boundary layer. Thus the coagulation term calculated based on the average size distribution for each circle in layer 1 will dominate $\langle Q_s \rangle_1$ and is included in the calculated values of $w_e^{2 \rightarrow 1}$.

Thus we conclude that the most probable source of the particles in this mode is transport from the buffer layer, where particles exist at the 20-nm mode at a concentration of 300 cm^{-3} . The particles in this mode in the PBL and buffer layer circles are each integrated to calculate the change in particle number as a function of time, $\langle \partial S / \partial t \rangle_1$, as well as the difference in particle concentration across interface A, δS_A . The lower bound for integration is taken as 10 nm, and the upper bound is calculated for both 20 and 30 nm. The difference in the integral values for the two upper bounds was minimal, and the 30-nm upper bound was found to more accurately represent the concentration increase for the mode since it included a more complete fraction of the mode's particles. The resulting changes in the modal concentration with time are shown in Figure 20, along with the measured value of δS_A from equation (24). Using these values and the expressions for $h(t)$ given in equation (20) and (21) above, equation (15) then provides the estimates of entrainment rates from the buffer layer into the PBL.

Figure 20 shows that the entrainment rates increase from near zero at the start of flight 24 to 0.012 m s^{-1} during flight 26. As expected for a well-mixed PBL, there is little difference in the rates predicted using the 30 and 150 m data sets.

3.4.2. DMS transport. Measurements of DMS from the aircraft provided an effective tracer for trans-

port from the PBL to the buffer layer, since the only source of DMS is emission from the sea surface. Oxidation of DMS in the atmosphere by OH radicals provides a diurnally varying sink for DMS and limits the lifetime of DMS in the troposphere to a few days. Because of this, concentrations of DMS in the buffer layer are lower than the PBL, and concentrations above interface B (in the free troposphere) are lower than in layer 2. Hence knowing the DMS oxidation rate and mean concentration allows DMS to be used as a tracer for estimating $w_e^{1 \rightarrow 2}$. We also use the mixed-layer gradient technique to estimate surface flux of DMS and hence to estimate $w_e^{2 \rightarrow 1}$.

DMS concentrations were calculated from 3-min integrated samples collected approximately every 5 min in the NCAR C130 flights during ACE 1 [Bandy and Thornton, 1996]. For each circle, a value was calculated by averaging four to six measurements collected at a single altitude. These values are plotted in Figure 21 and were fit with quadratic curves using the least squares method. At 30 and 150 m, DMS concentrations are similar, with means of 80 to 120 parts per trillion by volume (pptv) which increase during Lagrangian B. At 900 to 1200 m, DMS concentrations are initially lower at 20 pptv, but increase steadily. DMS concentrations above interface B, measured at 1500 to 2100 m, were frequently below the sampling detection limit (~ 1 pptv), but showed an average of 15 pptv at 2311 December

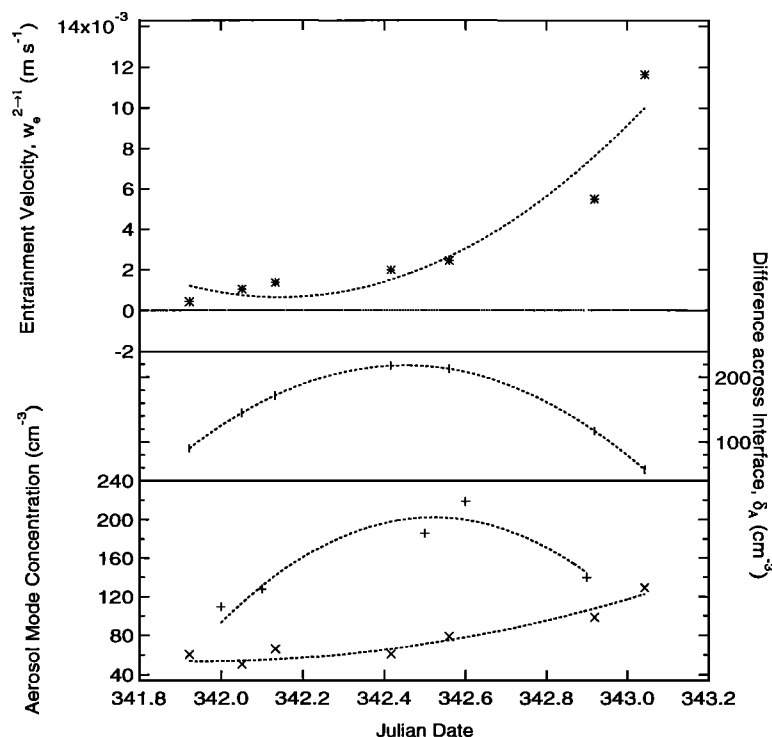


Figure 20. The top left axis shows entrainment velocities of air from layer 2 to layer 1 calculated by the increase in particles observed in layer 1 at 150 m in the size range of 10 to 30 nm. The middle right axis plots the difference between layers 2 and 1, or δ_A . The bottom left axis shows the integrated modal concentrations of particles in the range of 10 to 30 nm as functions of time at altitudes of (a) 900 to 1200 m (+’s) and (b) 150 m (x’s).

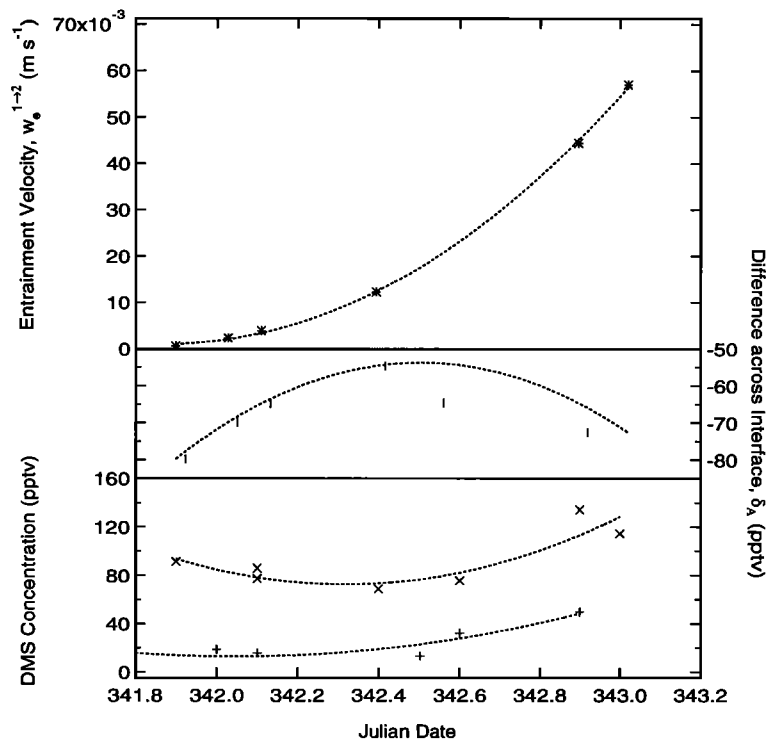


Figure 21. The top left axis shows entrainment velocities of air from layer 1 to layer 2 calculated by the increase in DMS observed in layer 2 at 900 m. The middle right axis plots the difference between layers 2 and 1, or δ_A . The bottom left axis shows the DMS concentrations as functions of time at altitudes of (a) 900 to 1200 m (+s) and (b) 150 m (x's).

8, 1995 (flight 26). Because the measurements at this level were limited, we will assume that the ratio of DMS concentration at level B_+ (in the free troposphere) to that at B_- (in the buffer layer) is constant and equal to 0.60, which is the value obtained from measurements at 2311 December 8, 1995.

A lower bound on the value of $w_e^{1 \rightarrow 2}$ can be estimated directly by equation (16) from the changes in DMS concentration and the vertical difference across the boundary layer top, as plotted in Figure 21. To obtain a more accurate estimate, the primary sink of DMS by oxidation with OH was used to correct the DMS concentrations. For this calculation the measurements of F. Eisele and L. Mauldin (personal communication, 1997) were used. The largest impact of this correction is during the daylight hours of flight 24, since flight 25 occurred during night hours and flight 26 was overcast, resulting in much lower OH concentrations.

3.5. Divergence Calculations

For each circle, the lateral component v_n (that is, normal to the flight path) of the wind vector was integrated around the closed flight path to provide an estimate of the mean horizontal flow divergence at that altitude [Lenschow, 1996]. Clockwise and counterclockwise circles were flown so that the mean bias in v_n is removed by averaging. The mean vertical motion at interface A (W_{h_A}) is then obtained by integrating the

mean divergence estimates from the surface up to h_A equation (17). The uncertainty associated with this approach was evaluated by Lenschow [1996].

The net entrainment velocity w_e^A is then estimated from equations (22) and (3). The results are plotted in Figure 22. The velocity w_e^A decreases from 0.04 to -0.04 m s^{-1} which compares well with the trend in the aerosol- and DMS-calculated entrainment rates. The decrease in net downward entrainment from an initial value of 0.04 m s^{-1} for the divergence method to 0 at flight 25 and to -0.04 m s^{-1} (net upward) during flight 26 is consistent with the rapid increase in $w_e^{1 \rightarrow 2}$ (as estimated from the DMS concentration in the buffer layer as Ri_B decreases) compared to $w_e^{2 \rightarrow 1}$, which also increases but not as much as $w_e^{1 \rightarrow 2}$ (as estimated by the particle concentration in the PBL).

Figure 23 compares the four methods we have to estimate the entrainment between the buffer layer and the free troposphere. All of the flux methods predict values near zero, whereas the divergence method shows an entrainment rate increasing to 0.08 m s^{-1} .

3.6. DMS Flux

The measurements collected in ACE 1 also provide a unique opportunity to compare three independent methods of estimating the flux of DMS at the ocean surface. The first method uses the seawater concentration of DMS and a sea-air transfer velocity to estimate a

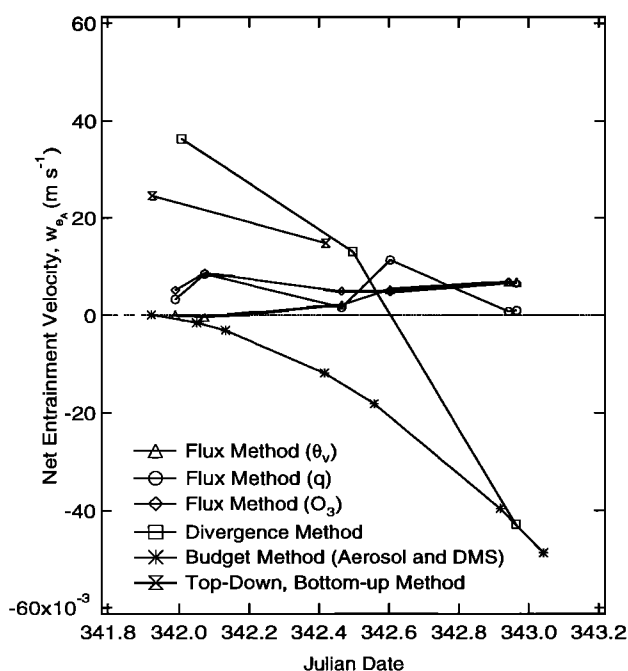


Figure 22. Estimated net entrainment velocities, w_{eA} , calculated from four different methods: (1) flux method for virtual potential temperature, for water mixing ratio and for ozone, (2) divergence method, (3) budget method, and (4) the mixed-layer gradient method.

flux based on mean wind speed at approximately 10 m. Two such parameterizations that have been proposed [Liss and Merlivat, 1986; Wanninkhof, 1992] differ by approximately a factor of 2 for the flux estimates result-

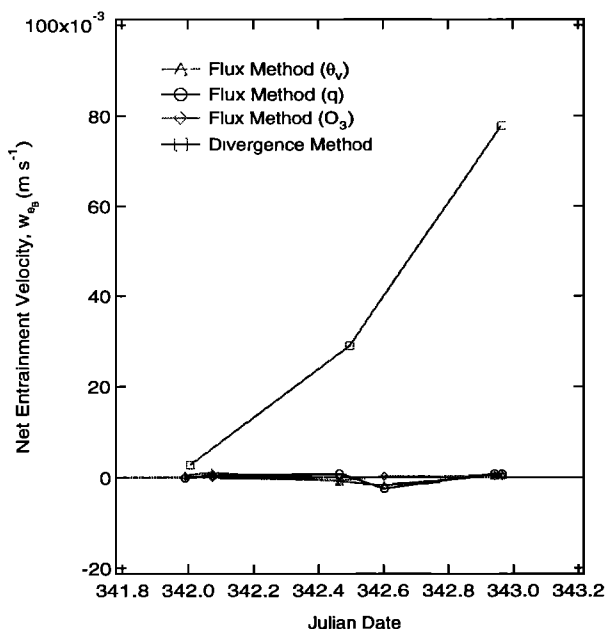


Figure 23. Estimated net entrainment velocities, w_{eB} , calculated from two different methods: (1) flux method and (2) divergence method.

ing from our data, with the Liss and Merlivat [1986] estimates providing the consistently lower values [Bates *et al.*, this issue (b)]. For the conditions measured here, we have chosen to use the Liss and Merlivat based estimates since they give better agreement with the other techniques, and these are illustrated in Figure 24. However, we note that the discrepancy between the fluxes from the two parameterizations suggests the magnitude of the uncertainty associated with estimates based on this method.

The second method of estimating DMS flux for which data were available in the ACE 1 measurements is the application of the top-down, bottom-up mixed layer approach [Moeng and Wyngaard, 1989] to the average atmospheric DMS concentrations at multiple levels to give the concentration gradient in the boundary layer. In this method, the results of representative runs of a Large Eddy Simulation (LES) model are used to parameterize the relative magnitudes of the contributions of bottom-up (surface) and top-down (entrainment) fluxes to the mixed-layer gradient. For flights 24 and 25 convective LES-derived parameterizations were used, but in flight 26 the boundary layer was shear-driven, so a different set of parameterizations were employed (C. Moeng, unpublished results, 1997). By using three levels of DMS measurements, spread from near the surface to near the top of the boundary layer, we have obtained estimates of both surface flux and entrainment rates for two stacks during the Lagrangian, whereas for the remaining four stacks, in which only two altitudes were measured in the boundary layer, we have used the approximation that for the lowest flight levels at 30 and 150 m the gradient is primarily determined by the bottom-up flux and have neglected entrainment. These estimates are also included in Figure 24.

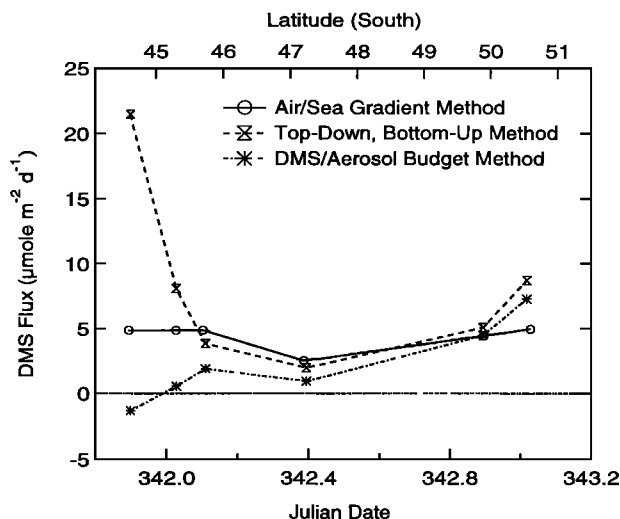


Figure 24. Comparison of DMS flux at the ocean surface as calculated by three methods, namely (1) air/sea gradient, (2) top-down, bottom-up, and (3) DMS/aerosol budget methods.

The third method employs a budget approach to the DMS concentration and incorporates our calculation of $w_e^{2 \rightarrow 1}$. Rearranging equation (15), we have

$$(\overline{ws})_0 = h_A \left(\left\langle \frac{\partial S}{\partial t} \right\rangle_1 - \langle Q_s \rangle_1 \right) - w_e^{2 \rightarrow 1} \delta S_A. \quad (32)$$

The change in concentration in layer 1 and the sources and sinks of DMS are calculated from the measured DMS values, and $w_e^{2 \rightarrow 1}$ is obtained from the nucleation-mode aerosol budget method estimate shown in Figure 20. The resulting estimates of DMS flux by this budget method are also shown in Figure 24.

A comparison of these three different methods of calculating flux shows quite good agreement in the calculated magnitude of the flux for four of the six stacks of measurements. The primary discrepancy in the methods is in the first two stacks of flight 24 where the top-down, bottom-up boundary layer gradient method provides a high estimate of $20 \mu\text{mol m}^{-2} \text{d}^{-1}$. This value reflects a single circle with an anomalously high atmospheric DMS measurement for the flight. This anomaly may be due in part to spatial inhomogeneities associated with the recent frontal passage.

The top-down, bottom-up method can in principle also provide an estimate of entrainment in cases with three or more measurements per stack. There are two such cases here: stack 1 of flight 24 and stack 1 of flight 25. For stack 1 of flight 24 we have used measurements at 150, 320, and 480 m as those altitudes appeared less influenced by the spatial inhomogeneities in DMS noted above. For stack 1 of flight 25, the three levels available were 30, 150, and 470 m. The resulting two predicted net entrainment values are plotted in Figure 22.

4. Discussion

Evidence from aerosol and DMS evolution data clearly shows bidirectional transport across the top of the PBL that increases during the third flight of the Lagrangian which occurred between 26 and 34 hours after the tetroons were launched. The observed structure is illustrated in Figure 1. These data are consistent with the divergence-derived estimates of net entrainment (w_e^A), as well as with the DMS-derived upward entrainment ($w_e^{1 \rightarrow 2}$) during the third flight which exceeds the aerosol-derived downward entrainment ($w_e^{2 \rightarrow 1}$), and is consistent with a net negative entrainment rate of up to $w_e^A = -0.040 \text{ m s}^{-1}$. The decreasing hydrodynamic stability, as estimated by a bulk Richardson number, supports this conclusion.

Probably the most critical variable in determining the accuracy of the budget technique for estimating the entrainment rates is the jump in concentration across the layer interfaces, since it appears in the denominators of equations (15) and (16). If the jump is small, the accuracy is compromised, both by sampling limitations and sensor precision. Therefore the technique is best suited to relatively short-lived tracers (to enhance

the jump across layer interfaces) but which have a relatively long lifetime compared to the turbulent mixing timescale (so that the layer concentration is reasonably uniform). This means a lifetime of more than a couple of hours, but less than a couple of weeks. In this experiment, both DMS and submicron aerosol fall into this category. Since DMS surface flux can be estimated by the mixed-layer gradient method, DMS can be used as a tracer for both the flux and the budget method in the boundary layer. On the other hand, since the magnitude of the submicron aerosol source in the buffer layer is unknown, it could not be used to estimate entrainment from the boundary layer to the buffer layer.

We also note that a central assumption in the Lagrangian budget method employed here is that horizontal advection can be ignored. Although there was no strong evidence from the tracer measurements in the circle patterns of horizontal heterogeneity, the significant shear, particularly during flight 26, indicates that the difference in the advection rates of the boundary and buffer layers could be a significant source of error in the method we have used here.

Prediction of entrainment rates via the mixed-layer gradient method relies on LES parameterizations without bidirectional entrainment, so we have no basis for knowing from LES whether it has any appreciable impact on the formulations. However, as illustrated in Figure 22, the resulting entrainment velocities are consistent with the budget and tracer methods for the two sampling times for which sufficient DMS concentration differences were available. Furthermore, the turbulence measurements indicate that the entrainment processes, especially $w_e^{1 \rightarrow 2}$ in clear air, are likely to be dominated by sparsely distributed episodic events involving relatively small-scale eddies. Once the fluid is entrained into the boundary layer, eddies that extend throughout the boundary layer mix the entrained air downward. This feature suggests that the two entrainment processes are likely to be nearly independent (as suggested by Turner [1968], and thus that the top-down formulation may still be applicable in the bidirectional case. It would be desirable to confirm this, as well as other aspects of bidirectional entrainment with further LES experiments.

From equation (8), the net entrainment velocities w_e^A estimated from measurements of virtual potential temperature, ozone, and humidity fluxes are positive and of smaller magnitude than indicated by the aerosol, DMS, and divergence data in Figure 20. However, the magnitude of the estimates from the three flux methods are relatively consistent, varying between about 0 and 0.01 m s^{-1} . The probable causes for this discrepancy are (1) the measurement errors inherent in estimating fluxes at the interface through extrapolation of fluxes measured at lower levels to the interface, (2) the small magnitude and consequent large relative uncertainty associated with the estimates of the jump in concentrations across interface A, and (3) the assumption of a discon-

tinuous jump. As illustrated in the soundings in Figures 3, 4, and 5, the concentration gradient is neither steep nor distinct, and the magnitude of the concentration change is small relative to the measurement precision. Therefore we do not have high confidence in the results.

The estimates from the flux method for w_e^B show similar disagreement, likely for the same reasons. In addition, the flux method has another problem: the intermittency of the turbulence in the buffer layer. The values obtained by the flux method are again much smaller in magnitude than calculated from the divergence and the budget methods. In view of the rapid increase of h_B with time toward the end of the observation period, the flux method estimates are not credible. Thus, for this case, we conclude that the flux method is not useful for evaluating entrainment, while the budget (aerosol and DMS), top-down, bottom-up, and divergence methods provided consistent estimates and appear to be reliable. In addition, the budget method has provided a unique way to evaluate bidirectional entrainment velocities. By using this technique, we have evidence for the first time of turbulent entrainment in two directions across an interface at the top of the boundary layer.

Acknowledgments. LMR is indebted to the NCAR Advanced Study Program for providing for support this analysis. The aerosol measurements on which this work was based were supported by NSF grant ATM-9614105. DHL thanks Bob Gall of the NCAR Microscale and Mesoscale Meteorology Division (MMM) for supporting his participation in ACE 1. The National Center for Atmospheric Research (NCAR) is sponsored by the National Science Foundation. The authors express their gratitude to all those who contributed to the ACE 1 program. This work would not have been possible without the cooperation and support of the NCAR Atmospheric Technology Division (ATD), the crew of the NCAR C-130, the officers and crew of the NOAA ship *Discoverer*, and the Australian Bureau of Meteorology. This research is a contribution to the International Global Atmospheric Chemistry (IGAC) Core Project of the International Geosphere-Biosphere Programme (IGBP) and is part of the IGAC Aerosol Characterization Experiments (ACE).

References

- Albrecht, B.A., A model of the thermodynamic structure of the trade-wind boundary layer, II, Applications, *J. Atmos. Sci.*, **36**, 90–98, 1979.
- Bandy, A.R., and D.C. Thornton, Sulfur dioxide and dimethylsulfide measurements in ACE 1, paper presented at the American Geophysical Union Fall Meeting, San Francisco, Calif., Dec. 15–19, 1996.
- Bates, T.S., B.J. Huebert, J.L. Gras, F.B. Griffiths, and P.A. Durkee, The International Global Atmospheric Chemistry (IGAC) Projects' First Aerosol Characterization Experiment (ACE 1): Overview, *J. Geophys. Res.*, this issue (a).
- Bates, T.S., V.N. Kapustin, P.K. Quinn, D.S. Covert, D.J. Coffman, C. Mari, P.A. Durkee, W. J. De Bruyn, and E.S. Saltzman, Processes controlling the distribution of aerosol particles in the marine boundary layer during ACE 1, *J. Geophys. Res.*, this issue (b).
- Cotton, W.R., G.D. Alexander, R. Hertenstein, R.L. Walko, R.L. McAnelly, and M. Nicholls, Cloud venting – A review and some new global annual estimates, *Earth Sci. Rev.*, **39**, 169–206, 1995.
- Fernando, H.J.S. and J.C.R. Hunt, Turbulence, waves and mixing at shear-free density interfaces, 1, A theoretical model, *J. Fluid Mech.*, **347**: 197–234, 1997.
- Hainsworth, A.H.W., A.L. Dick, and J.L. Gras, Climatic context of ACE 1: A meteorological and chemical overview, *J. Geophys. Res.*, this issue.
- Huebert, B.J., A. Pszenny, and B. Blomquist, The AS-TEX/MAGE Experiment, *J. Geophys. Res.*, **101**, 4319–4329, 1996.
- Kawa, S.R., and R. Pearson, Ozone budgets from the dynamics and chemistry of marine stratocumulus experiment, *J. Geophys. Res.*, **94**, 9809–9817, 1989.
- LeMone, M.A., The marine boundary layer, in *Workshop on the Planetary Boundary Layer*, edited by J.C. Wyngaard, 322 pp., Am. Meteorol. Soc., Boston, Mass., 1980.
- Lenschow, D.H., Micrometeorological techniques for measuring biosphere-atmosphere trace gas exchange, in *Biogenic Trace Gases: Measuring Emissions from Soil and Water*, edited by P.A. Matson and R. C. Harriss, Chap. 5, pp. 126–163, Blackwell Sci., Cambridge, Mass., 1995.
- Lenschow, D.H., A proposal for measuring entrainment into the cloud-capped boundary layer, in *Proceedings of the ETL/CSU Cloud-Related Process Modeling and Measurement Workshop, Boulder, Colorado, 23–25 October 1995*, edited by A.S. Frisch, D.A. Randall, and W.H. Schubert. *NOAA ETL Report*, pp. 29–55, Natl. Oceanic and Atmos. Admin., Silver Spring, Md., 1996.
- Lenschow, D.H., I.R. Paluch, A.R. Bandy, R. Pearson, S.R. Kawa, C.J. Weaver, B.J. Huebert, J.G. Kay, D.C. Thornton, and A.R. Driedger III, Dynamics and chemistry of marine stratocumulus (DYCOMS) experiment, *Bull. Am. Meteorol. Soc.*, **69**, 1058–1067, 1990.
- Liss, P.S., and L. Merlivat, Air-sea gas exchange rates: Introduction and synthesis, in *The Role of Air-Sea Exchange in Geochemical Cycling*, edited by P. Buat-Menard, pp. 113–127, Reidel, Norwell, Mass., 1986.
- McGrath, J.L., H.J.S. Fernando, and J.C.R. Hunt, Turbulence, waves and mixing at shear-free density interfaces, 2, Laboratory experiments, *J. Fluid Mech.*, **347**, 235–261, 1997.
- Moeng, C.-H., and J.C. Wyngaard, Evaluation of turbulent transport and dissipation closures in second-order modelling, *J. Atmos. Sci.*, **46**, 2311–2330, 1989.
- Morley, B.M., K.K. Laursen, L.F. Radke, and A.D. Clarke, Early results from the Aerosol Characterization Experiment 1 using airborne lidar and in situ aerosol sampling, paper presented at the Second International Airborne Remote Sensing Conference and Exhibition: Technology, Measurement and Analysis, 24–27 June 1996, San Francisco, Calif., June 24–27, 1996.
- Russell, L.M., M.R. Stolzenburg, S.H. Zhang, R. Caldow, R.C. Flagan and J.H. Seinfeld, Radially-classified aerosol detector for aircraft-based submicron aerosol measurements, *J. Atmos. Oceanic Technol.*, **13**, 598–609, 1996.
- Schwiesow, R.L., S.D. Mayor, V.M. Glover and D.H. Lenschow, Intersection of a sloping aerosol layer observed by airborne lidar with a cloud-capped marine boundary layer, *J. Appl. Meteorol.*, **29**, 1111–1119, 1990.
- Smith, S.D., Coefficients for sea surface wind stress, heat flux, and wind profiles as a function of wind speed and temperature, *J. Geophys. Res.*, **93**, 15,467–15,472, 1988.
- Stull, R.B., *An Introduction to Boundary Layer Meteorology*, 670 pp., Kluwer Acad., Norwell, Mass., 1988.
- Turner, J.S., The influence of molecular diffusivity on turbulent entrainment across a density interface, *J. Fluid Mech.*, **33**, 639–656, 1968.
- Wang, Q., and D.H. Lenschow, An observational study

of the role of penetrating cumulus in a marine strato-cumulus-topped boundary layer, *J. Atmos. Sci.*, 52, 2778-2787, 1995.

Wanninkhof, R., Relationship between wind speed and gas exchange over the ocean, *J. Geophys. Res.*, 97, 7373-7382, 1992.

Lynn M. Russell, Department of Chemical Engineering, A317 Engineering Quadrangle, Princeton University, Princeton, NJ 08540. (e-mail: lrussell@princeton.edu)

Donald H. Lenschow and Krista K. Laursen, National Center for Atmospheric Research, P.O. Box 3000, Boulder, CO 80307. (e-mail: lenschow@ucar.edu; krista@raf.atd.ucar.edu)

Paul B. Krummel, CSIRO Division of Atmospheric Research, Private Bag 1, Aspendale, Victoria 3195, Australia. e-mail: paul.krummel@dar.csiro.au

Steven T. Siems, Department of Mathematics, Monash University, Clayton, Victoria 3168, Australia. (e-mail: siems@monsoon.maths.monash.edu.au)

Alan R. Bandy and Donald C. Thornton, Department of Chemistry, Drexel University, Philadelphia, PA 19104. (e-mail: arb@ac1.chemistry.drexel.edu; dct@ac2.chemistry.drexel.edu)

Timothy S. Bates, Pacific Marine Environmental Laboratory, National Oceanic and Atmospheric Administration, 7600 Sand Point Way NE, Seattle, WA 98115. (e-mail: bates@pmel.noaa.gov)

(Received June 9, 1997; revised November 11, 1997; accepted November 18, 1997.)